npj | energy materials

Article

https://doi.org/10.1038/s44456-026-00006-4

# Induced effect regulation of Nasicon-Type polyanion cathodes toward high-energy Na-ion batteries

Check for updates

Chunliu Xu[1,2], Yongchun Li[3], Guilin Feng[1], Zhao Chen[4], Xiaowei Li[1], Zhenguo Wu[5], Weiqing Yang[2] ✉, Xiaodong Guo[5] ✉, Junmei Zhao[1,6] ✉ & Yong-Sheng Hu[4] ✉

Iron-based NASICON-type polyanion materials are regarded as one of the most promising cathodes because of their low cost, three-dimensional $Na^+$ ion diffusion and robust structure stability for Na-ion batteries. However, the energy density of NASICON-type polyanion cathodes is greatly restricted by low $Fe^{2+}/Fe^{3+}$ redox potential, which is intrinsically dependent on the chemical coordination nature of the polyanion groups. Herein, the induced effects are carefully regulated by $SO_4/PO_4$ polyanions substitution engineering to maintain favorable kinetics and elevate $Fe^{2+}/Fe^{3+}$ redox potential. The reduced Fe-O covalency can enlarge energy gap between antibonding orbital and Fermi energy level, finally increasing the potential of $Fe^{2+}/Fe^{3+}$ redox couples. As concept proof, NASICON-type $Na_{0.6}Fe_2(PO_4)_{0.6}(SO_4)_{2.4}$ with suitable $SO_4/PO_4$ polyanion groups ratio delivers the enhanced induced effects with facilitated $Na^+$ migration kinetics, which enables an increased average working voltage of ~3.2 V (*vs.* ~ 2.8 V of $NaFe_2(PO_4)(SO_4)_2$ and ~2.45 V of $Na_3Fe_2(PO_4)_3$), achieving 400 W h $kg^{-1}$-level energy density.

Electric energy storage system (EES) provides an effective route to smoothly utilize various intermittent green energy sources[1,2]. Na-ion batteries (NIBs) are expected to meet the increasing demands for large scale EES and power grids considering their high safety, wide temperature adaptability and huge abundance of sodium sources. However, exploiting suitable cathode materials with low cost and high performance are still the main bottlenecks for practical NIBs[3,4]. NASICON-type polyanion cathodes are promising for NIBs owing to the favorable ion conduction and superior structure stability depending on three-dimensional (3D) and robust framework structure built by $MO_6$ (M represents transition metals) octahedra and $XO_4$ (X refers to P, S, Si, As, Mo, W, etc.) tetrahedra basic unites in a corner-sharing way[5,6]. Typically, NASICON-structured $Na_3V_2(PO_4)_3$ (where M = V, X = P, denoted as NVP) cathodes have demonstrated decent rate performance and long-term stability[7,8]. Nonetheless, the high cost and toxicity of vanadium in NVP finally limits its further application[9–12]. As a cost-effective choice, the benign and cheap iron-based $Na_3Fe_2(PO_4)_3$ (NFP) have received particular research interests due to the similar NASICON structure with NVP[13–15]. Unfortunately, the $Fe^{2+}/Fe^{3+}$ redox couples in NFP are only placed at ~2.45 V (hereinafter *vs.* $Na/Na^+$)[16,17], making NFP less attractive as a cathode, which is determined by the chemical nature of the polyanion $PO_4$ groups. It has been well established that the weakness or strengths of the covalency of the M-O bonds are at the origin of $M^{n+}/M^{n+1}$ redox voltage differences[6,13,18]. In the NASICON structure system, each center metal M has six M-O-X bond sequences and the inductive effect of $XO_4$ groups can adjust the covalency of the M-O bonds according to the electronegativity of X[6]. Based on this, the substitution of higher-electronegativity S for P in terms of polyanion groups can attract the electron cloud around the shared oxygen atom in Fe-O-P(S) bond, thereby weakening the covalent strength of Fe-O bond in the other end, finally increasing the $Fe^{2+}/Fe^{3+}$ redox voltage[19]. In response, in 2016, John B. Goodenough's group reported the $NaFe_2PO_4(SO_4)_2$ cathode for NIBs through polyanion substitution engineering[20], which can increase the average discharge voltage of $Fe^{2+}/Fe^{3+}$ redox couples over 2.8 V, greatly improving the energy density. However, when $PO_4$ polyanions are further completely replaced by sulfate ($SO_4$) groups, the working voltage of the obtained $Na_xFe_2(SO_4)_3$ cathode showed no significant increase due to large electrochemical polarization and voltage

[1]CAS Key Laboratory of Green Process and Engineering, Institute of Process Engineering, Chinese Academy of Sciences, Beijing, China. [2]Research Institute of Frontier Science, Key Laboratory of Advanced Technologies of Materials (Ministry of Education), School of Materials Science and Engineering, Southwest Jiaotong University, Chengdu, China. [3]Ångström Laboratory, Department of Chemistry, Uppsala University, Uppsala, SE, Sweden. [4]Key Laboratory for Renewable Energy, Beijing Key Laboratory for New Energy Materials and Devices, Beijing National Laboratory for Condensed Matter Physics, Institute of Physics, Chinese Academy of Sciences, Beijing, China. [5]School of Chemical Engineering, Sichuan University, Chengdu, China. [6]College of Chemistry, Xinjiang University, Urumqi, China. ✉e-mail: wqyang@swjtu.edu.cn; xiaodong2009@scu.edu.cn; jmzhao@ipe.ac.cn; yshu@iphy.ac.cn

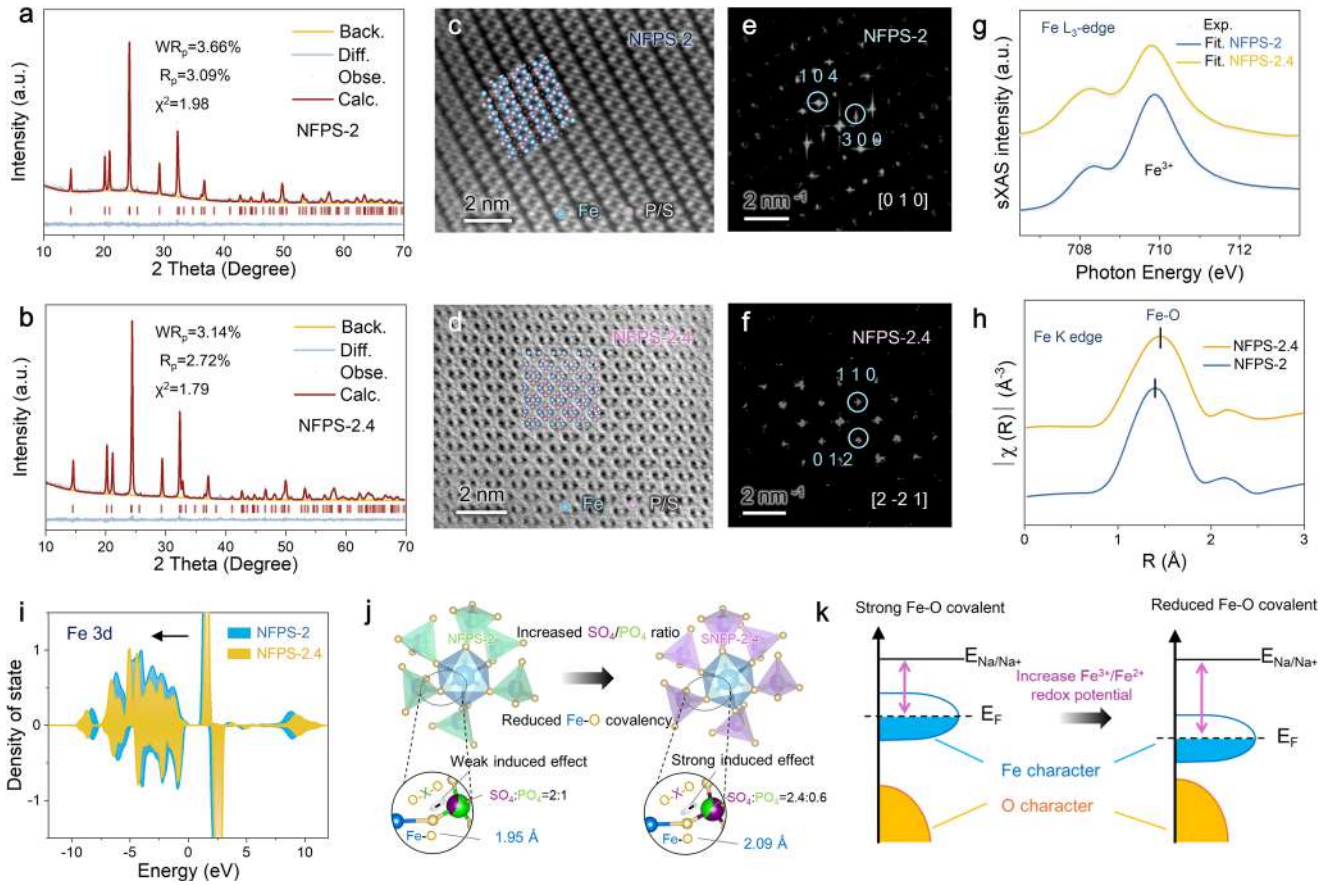



**Fig. 1 | Material structure characterizations.** XRD Rietveld refinements of NFPS-2 (**a**) and NFPS-2.4 (**b**) powder. The STEM images (**c**, **d**) and SAED patterns (**e**, **f**) for NFPS-2 and NFPS-2.4 samples. The insets in Fig. 1c and d are their corresponding crystal structure model along with axis zone directions. **g** The fitted XAS spectra at Fe L edges of two samples. **h** The EXAFS spectra at Fe K edges of two cathodes. **i** The partial DOS of Fe 3 d for NFPS-2 and NFPS-2.4 cathodes. **j** The bond length variation of Fe-O caused by the induced effects from different $SO_4^{2-}/PO_4^{3-}$ ratio. **k** Schematic illustration of molecular orbit changes induced by the different covalency of Fe-O.

hysteresis, which could be associated with the sluggish electrochemical kinetics caused by excess $SO_4^{2-}$ polyanions in structure[21,22]. The small size of $SO_4^{2-}$ anions can lower structure symmetry, thus limiting the site availability and the mobility of $Na^+$ ions in the NASICON phase. The further regulation of induced effect by optimizing the relative ratio of $SO_4/PO_4$ polyanion group is expected to elevate the $Fe^{2+}/Fe^{3+}$ redox potential without deteriorating kinetics, thereby increasing the energy density. However, there are few reports on the new NASICON-type mixed $SO_4$-$PO_4$ polyanion cathodes, therefore missing the opportunity to achieve higher working voltage and energy density.

In this work, by appropriately increasing the proportion of $SO_4/PO_4$ mixed polyanion groups, we have developed a new NASICON type iron-based polyanion cathode material ($Na_{0.6}Fe_2(PO_4)_{0.6}(SO_4)_{2.4}$, NFPS-2.4), which enables an increased working voltage (*vs.* $NaFe_2PO_4(SO_4)_2$, NFPS-2) based on $Fe^{2+}/Fe^{3+}$ redox couples due to the reduced Fe-O covalency characteristics determined by the induced effect regulation of polyanion groups. More $SO_4$ polyanions possess stronger electron-withdrawing ability from oxygen atoms, that is enhanced induced effect, which can diminish the covalency of the Fe-O bonds and lower the energy of the antibonding states, hence increasing the potential difference between the $Fe^{2+}/Fe^{3+}$ and the $Na/Na^+$ redox couples. As a result, the new NASICON-type NFPS-2.4 cathode can deliver an average discharge voltage of ~3.2 V and hence increase the energy density to 400 W h $kg^{-1}$ level, which is higher than other iron-based polyanion cathodes, even including orthorhombic-phase $Na_4Fe_3(PO_4)_2P_2O_7$ and alluaudite-polymorph $Na_3Fe_2(SO_4)_3$. Besides, our findings also indicate that NFPS-2.4 can maintain robust structure framework and facilitated ion conduction during de/sodiation due to appropriate $SO_4/PO_4$ mole ratio in NASICON structure. Consequently, even at high rate of 10 C, the designed NFPS-2.4 cathode still allows a high reversible capacity of ~90 mA h $g^{-1}$ and superior cycling performance with 83% capacity retention after ~3000 cycles. More importantly, favorable air/humidity stability and all-climate temperature tolerance were also demonstrated. Our current work provides new insight into increasing the $Fe^{2+}/Fe^{3+}$ redox voltage in NASICON-type polyanion cathodes, and the proposed NFPS-2.4 can be regarded as a promising cathode candidate for low-cost, long-life, all-climate and high-energy NIBs.

## Results

### Material characterizations

Figure 1a, b display X-ray diffraction (XRD) Rietveld refinements of NFPS-2 and NFPS-2.4 powder, in which the structural model of $NaFe_2PO_4(SO_4)_2$ with statistical disorder of P/S were used for the initial stimulation input. Considering the good fitting between experiment observation and calculation data with satisfactory reliability factors, the structures can be determined as typical NASICON-type phase with R-3c space group[20,23,24]. The thermogravimetric analysis (TGA) (Fig. S1) confirms that the carbon contents of two samples composites have approximately 4% (by weight), well consistent with the design values. Raman spectra show the characteristic peaks of D band (~ 1350 $cm^{-1}$) and G band (~1600 $cm^{-1}$) (Fig. S2), which reveals the $I_D/I_G$ values of NFPS-2 and NFPS-2.4 are equal at 1.11, reflecting the main disordered characteristics of Ketjen black (KB) carbon in two samples[25]. X-ray photoelectron spectroscopy (XPS) at C 1 s spectra reveals high proportion of C-C bond in two samples (Fig. S3), suggesting the

favorable electronic conductivity after mixing KB[26]. Scanning electron microscope (SEM) images indicate the micro-nanosized particle morphologies of NFPS-2 and NFPS-2.4 samples (Fig. S4). Furthermore, the crystal structures of samples at the atom level were observed by the aberration-corrected high-resolution scan transmission electron microscopy (STEM). Although the Na and O atomic reflection is relatively weaker, the Fe and P/S arrangements can be clearly captured. As shown in Fig. 1c, d, both STEM images of NFPS-2 and NFPS-2.4 can match well with R-3c symmetry in NASICON structures (inset), further confirming the high phase purity of the as-obtained materials. The corresponding selected area electron diffraction (SAED) patterns identify that the framework structures of NFPS-2 and NFPS-2.4 were viewed along with the direction of [0 1 0] (Fig. 1e) and [2 -2 1] (Fig. 1f), respectively. STEM-energy dispersive spectroscopy (EDS) mapping results (Fig. S5) indicate the coexistence and event distribution of Na, Fe, P, S and O elements included in NFPS-2.4 cathodes. The composition analysis of two samples was further investigated by inductively coupled plasma-optical emission spectroscopy (ICP-OES), which confirms their desirable element compositions close to the design values (Table S1). To determine the chemical oxidation state of iron in samples, soft X-ray absorption spectroscopy (sXAS) was employed in the total fluorescence yield (TFY) mode. The sXAS spectra at Fe $L_3$ edges of NFPS-2 and NFPS-2.4, presented in Fig. 1g, could be well fitted with the referenced $Fe^{3+}$ line in the six-coordinated oxygen environment, indicative of their trivalent features[27]. XPS spectra shows the characteristic peaks of Fe $2p_{1/2}$ and $2p_{3/2}$ orbits located at the energy position of ~725 and ~711 eV (Fig. S6), respectively, further confirming the $Fe^{3+}$ species in two samples. Besides, we measured the $^{57}$Fe Mössbauer spectrum of NFPS-2.4 sample under room temperature (Fig. S7), which also reveals Fe was mainly in the +3-oxidation states[22]. The local environments of Fe atoms in NFPS-2 and NFPS-2.4 were investigated by analyzing the extended X-ray absorption fine structures (EXAFS)[13]. It could be observed that the main Fe-O peak reflection of NFPS-2.4 has a weaker interatomic interaction than that of NFPS-2 (Fig. 1h). Figure 1i and Figure S8 compare the projective Fe 3 d and O2p state of density (DOS) of two cathodes, respectively, from the first-principles calculations. In comparation with NFPS-2 models, NFPS-2.4 shows a lowered energy shift in terms of Fe 3 d orbitals (Fig. 1i) but toward a higher energy position for the O 2p antibonding orbitals (Fig. S8), which implies that NFPS-2.4 has less hybridization between Fe 3 d and O 2p states and weaker covalency of Fe-O bond[28,29]. To further investigate the coordination environments variation of the Fe metal center with introduction of more $SO_4$ groups in structure, we summarize the structure details of NFPS-2 and NFPS-2.4 based on the XRD refinements (Table S2–3). The average bond length of P/S-O was calculated to be 1.509 Å and 1.476 Å in NFPS-2 and NFPS-2.4, respectively. Such a significant difference in bond length was mainly ascribed to the different induced effects determined by the relative content of $SO_4$ and $PO_4$ in structure[22,30]. Sulfur has stronger electron-withdrawing ability from oxygen atoms due to stronger electronegativity than phosphorus, thus allowing enhanced covalent bond[6]. Therefore, compared with NFPS-2, NFPS-2.4 with more $SO_4$ proportion finally contributes to a decreased average P/S-O bond length. On the other hand, as shown in Fig. 1j, the average bond distance of Fe-O (adjacent to P/S-O) will increase in the case of NFPS-2.4 cathode (2.09 Å *vs.* 1.95 Å in NFPS-2) to keep the lowest energy in structure, in good agreement with the above DOS results and EXAFS analysis. The reduced Fe-O covalency is of significance to increase the working voltage of $Fe^{2+}/Fe^{3+}$ redox couples[13]. As described in Fig. 1k and (Figure S9), compared to NFPS-2, the reduced covalent interaction between the Fe 3 d and O 2p orbitals for NFPS-2.4 cathode contributes to the enlarged energy gap between antibonding orbital and Fermi energy level, increasing its electrochemical potential between $Fe^{2+}/Fe^{3+}$ and the $Na/Na^+$ redox couples.

## Structure and dynamics

Given the structural variation induced by chemistry of $SO_4$ group, we further investigate the structure differences with increase of $SO_4$ proportion in the NASICON-structure $Na_{1-x}Fe_2(PO_4)_{1-x}(SO_4)_{2+x}$ ($0 \le x \le 1$, e.g., $x = 0, 0.2, 0.4, 0.6$ and 1) family. Typically, several samples were denoted as NFPS-2, NFPS-2.2, NFPS-2.4, NFPS-2.6 and NFPS-3 according to the content of $SO_4$ group in structure. Firstly, the Fourier transform infrared (FT-IR) data was collected to detect the chemical bond and group information of as-prepared samples (Fig. S10). The predominant band in the range of 950–1300 $cm^{-1}$ represents the symmetric stretching modes of the $SO_4$ units, indicating $SO_4$ polyanions as main groups in all samples[19]. Particularly, the peak around 465 $cm^{-1}$ corresponds to the bending vibrations of $PO_4$ group, whose intensity can reflect the relative content of $PO_4^{3-}$ in samples (Fig. 2a). Due to absence of $PO_4^{3-}$ polyanions in NFPS-3, no peak signal can be observed in such wavenumber range. On the contrary, the highest proportion of $PO_4$ group in NFPS-2 leads to its strongest peak reflection among several samples. Figure 2b displays the FTIR peaks between 570–670 $cm^{-1}$, which can be assigned to the stretching vibration of the Fe-O bond[31]. However, when $SO_4$ group increases to 2.6 mole (per formula), the Fe-O peak shape begins to vary obviously, indicating the sudden structure change due to incorporation of excess $SO_4$ groups. Such a structural mutation in $FeO_6$ octahedron coordination was also reflected by the Raman measurements (Fig. S11). NFPS-2, NFPS-2.2 and NFPS-2.4 exhibit the obvious characteristic Raman signals of $FeO_6$ coordination in the region of 100–350 $cm^{-1}$ (Fig. S11a). However, for comparison, the characteristic peaks located at ~170 $cm^{-1}$ in NFPS-2.6 and NFPS-3 have disappeared, indicative of the changed coordinative surroundings of Fe as more $SO_4$ groups included in structures[19,32]. The vibrational modes of the mixed polyanionic groups ($SO_4$ and $PO_4$) can be assigned to the multiple Raman peaks around 450 $cm^{-1}$ for all the samples (Fig. S11b). Further, we compare the XRD patterns of NFPS-2, NFPS-2.2, NFPS-2.4, NFPS-2.6 and NFPS-3 cathodes (Fig. S12), which shows, overall, all samples demonstrate similar NASICON-type phase structures. However, some changes in diffraction peak intensity and shifts in diffraction peak position can be observed, as presented in the enlarged locally enlarged XRD patterns. With the increased proportion of $SO_4$ group in structure, the relative peak intensity ratio of $I_{104}/I_{110}$ increases accordingly (Fig. 2c), which can be ascribed to a comprehensive contribution from small size and chemical features of $SO_4^{2-}$ anions. The structure shrinkage of polyanion units and $FeO_6$ octahedron distortion can change the arrangement and distribution of heavy Fe and P/S atoms, thus leading to intensity variation of some diffraction peak signal, such as (104) and (110) in our case[33,34]. It should be noted that the $I_{104}/I_{110}$ ratio displays an abrupt significant increase when $SO_4$ content increases from 2.4 mole (NFPS-2.4) to 2.6 mole (NFPS-2.6), which reveals the structure transition from R-3c to R-3 symmetry, accompanied by the splitting of Na, Fe, and O positions[20,22]. Consequently, NFPS-2, NFPS-2.2 and NFPS-2.4 samples were refined by adopting R-3c space group (Fig. 1a, b and Fig. S13), while NFPS-2.6 and NFPS-3 were stimulated using R-3 symmetry as structure model (Figures S14–15). All XRD Rietveld refinements exhibit good reliability factors. We note that the (110) and (211) diffraction peaks show significant shifts towards higher angles as the relative content of $SO_4$ group increases (Fig. 2c, d), which results from the decreased $Na^+$ number and reduced unit cell volume, in accord with their XRD refinements results (Table S2–6). Based on these observations, we can conclude that, in the $Na_{1-x}Fe_2(PO_4)_{1-x}(SO_4)_{2+x}$ family, an appropriate ratio of $SO_4/PO_4$ ($x \le 0.4$) can maintain R-3c symmetry, however, excess $SO_4$ groups ($x \ge 0.6$) can cause the lowered framework symmetry with possible structure distortion, leading to dynamics deterioration.

We calculated the energy barrier of $Na^+$ migration from the octahedral 3a to 3b sites along the interstitial space in several structure models based on the density functional theory (DFT) calculations[22]. Note that, instead of assigning $SO_4$ or $PO_4$ groups at specific sites, a random distribution of S/P is adopted according to a statistical result in our calculations. As shown in Fig. 2e, the activation energy barrier for $Na^+$ diffusion of NFPS-2 was calculated as 0.279 eV, indicating its favorable transfer kinetics. For comparison, NFPS-2.4 also shows a $Na^+$ migration energy barrier at a low level of 0.283 eV (Fig. 2f), which is comparable to that of NFPS-2 and even lower than our well-known $Na_3Fe_2(PO_4)_3$ (0.31 eV)[22]. However, with the further increase of the $SO_4/PO_4$ ratio to 2.6:0.4 in NFPS-

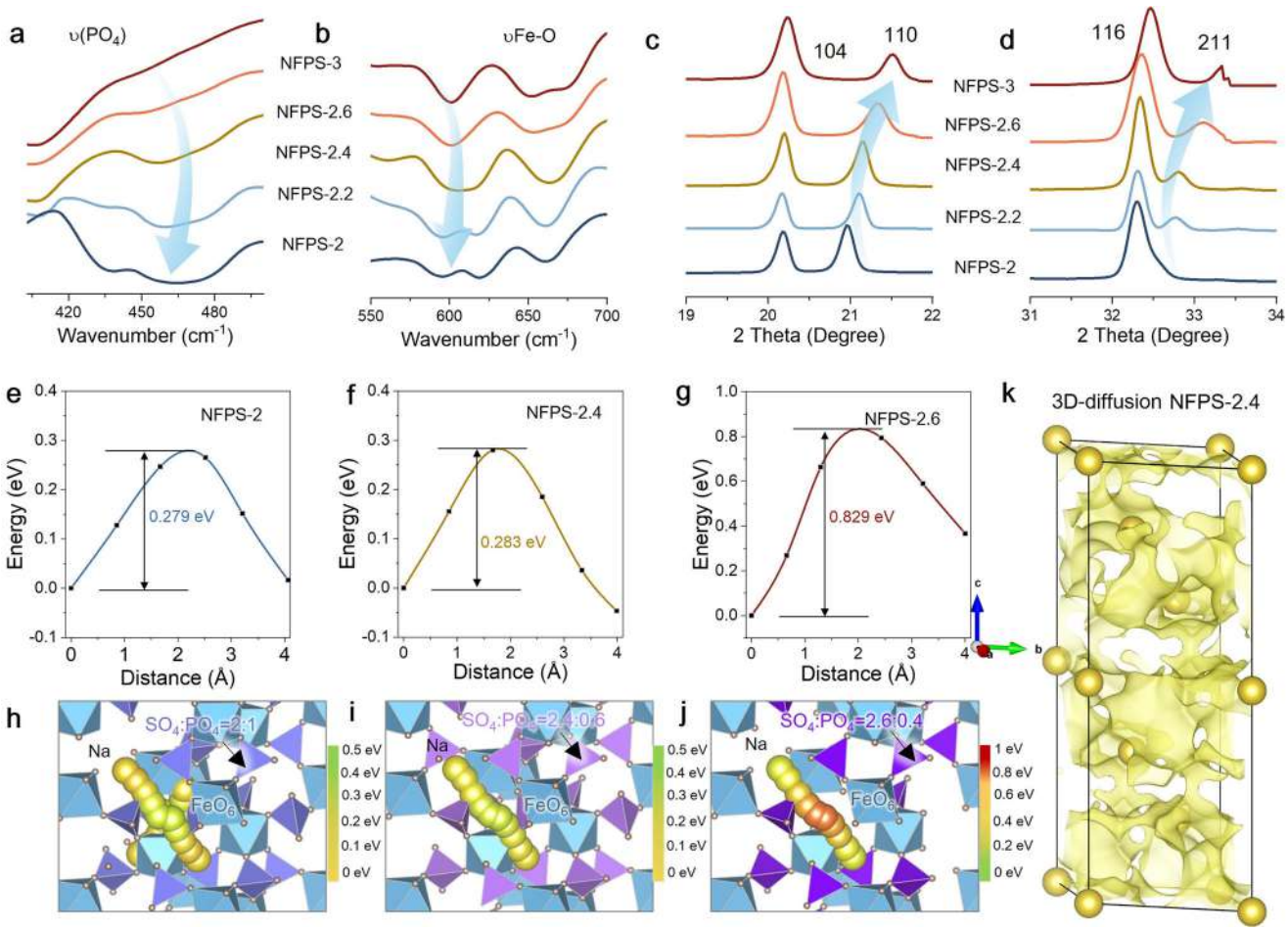



**Fig. 2 | The correlation between structure and dynamics.** FTIR spectra of $Na_{1-x}Fe_2(PO_4)_{1-x}(SO_4)_{2+x}$ family in the ranges of 400–495 $cm^{-1}$ (**a**) and 550–700 $cm^{-1}$ (**b**). XRD patterns of as-prepared samples in the ranges of 19–22 ° (**c**) and 31–34 ° (**d**). The $Na^+$ migration energy barriers of NFPS-2 (**e**) NFPS-2.4 (**f**) and NFPS-2.6 (**g**) models. The $Na^+$ migration pathway in NFPS-2 (**h**) NFPS-2.4 (**i**) and NFPS-2.6 (**j**) models. **k** Schematic illustrations of the possible migration pathways represented by the yellow isosurface in NFPS-2.4 structures.

2.6, owing to destruction of the structural symmetry caused by excess $SO_4$ groups, the $Na^+$ migration path from the 3b site to the intermediate 18 f site (R-3 space group) generated the bottleneck-like channels, leading to the energy barriers up to 0.829 eV (Fig. 2g). Similar $Na^+$ migration obstacles have been revealed in NFPS-3 cathodes reported by Yamada's group[22], which results in the limited $Na^+$ mobility and large electrochemical polarization. Although more $SO_4$ groups in structure with stronger induced effects can elevate the $Fe^{2+}/Fe^{3+}$ redox potential from the perspectives of molecular orbital and energy band theory, the degradation of $Na^+$ migration kinetics after introduction of excess $SO_4$ would lead to polarization and voltage hysteresis of cathode materials. Therefore, it is necessary to carefully control the proportion of $SO_4^{2-}$ anions in $Na_{1-x}Fe_2(PO_4)_{1-x}(SO_4)_{2+x}$ family to regulate the induction effects, meanwhile maintaining good $Na^+$ migration kinetics, ultimately achieving an increase in working voltage and energy density. As shown in Fig. 2h–j, deeper purple color reflects higher proportion of $SO_4^{2-}$ in polyanion groups, which shows the schematic illustration of $Na^+$ migration pathway of several cathodes with increase of $SO_4^{2-}$ content, representing the lowest energy positions of $Na^+$ migration between 3a and 3b sites. In the case of NFPS-2.4, we further calculated its possible $Na^+$ migration pathways represented by the yellow isosurface (set as1.0 eV) in the primitive structure models (Fig. 2k), which reveal a 3D and crosslinking $Na^+$ diffusion channel, demonstrating favorable dynamics. NFPS-2.4 cathodes were expected to deliver improved working voltage and energy density due to combination of the increased induced effects and facilitated $Na^+$ diffusion kinetics determined by the appropriate proportion of $SO_4$ groups in structure.

## Electrochemical performance

The electrochemical behavior was evaluated in half cells, in which the pre-discharging process was carried out to obtain Na compensation for NFPS-2 and NFPS-2.4 cathodes (Fig. S16). The loading of active substances in all electrode materials remains at 5 mg $cm^{-2}$ level, ensuring the reliability of the electrochemical results. Figure 3a compares the typical charging/discharging profiles of two cathodes at 0. 1 C (where 1 C is defined as 120 mA $g^{-1}$) between 2.0-4.4 V, which reveals their close reversible capacities of ~125 mA h $g^{-1}$, implying a two-electron reaction based on $Fe^{2+}/Fe^{3+}$ redox couples through reversible extraction/insertion of 2 mole $Na^+$ (per formula) in the NASICON framework. However, due to the increased induced effects from the appropriate proportion of $SO_4$ groups in structure, NFPS-2.4 achieves the working voltage increase from ~2.85 V to ~3.2 V (Fig. 3b), resulting in the energy density increase from ~360 to ~395 W h $kg^{-1}$. To our best knowledge, the current energy density of NFPS-2.4 cathode is higher than the representative iron-based polyanionic cathodes for NIBs (Fig. 3c), including $Na_2FePO_4F$[35], $Na_2Fe_2(SO_4)_3$[36], $Na_4Fe_3(PO_4)_2P_2O_7$[37], $Na_{3.32}Fe_{2.11}(P_2O_7)_2$[38], $Na_2FeP_2O_7$[39], $Na_3Fe_2(PO_4)_3$[17] and $NaFePO_4$ (olivine[15] or maricite phases[34]). Besides, compared with the other reported NFPS-2 materials[20,22–24,30], our proposed NFPS-2.4 cathodes with more $SO_4$ groups further demonstrate the beneficial advantages in terms of the induced effects to increase the working voltage and energy density, representing its significant advance.

To investigate the effects of $SO_4$ group content in NASICON structure on electrochemical behavior, we compare the discharging dQ/dV profiles of several cathodes (Fig. 3d). It can be found that, when $x \le 0.4$ in $Na_{1-}$

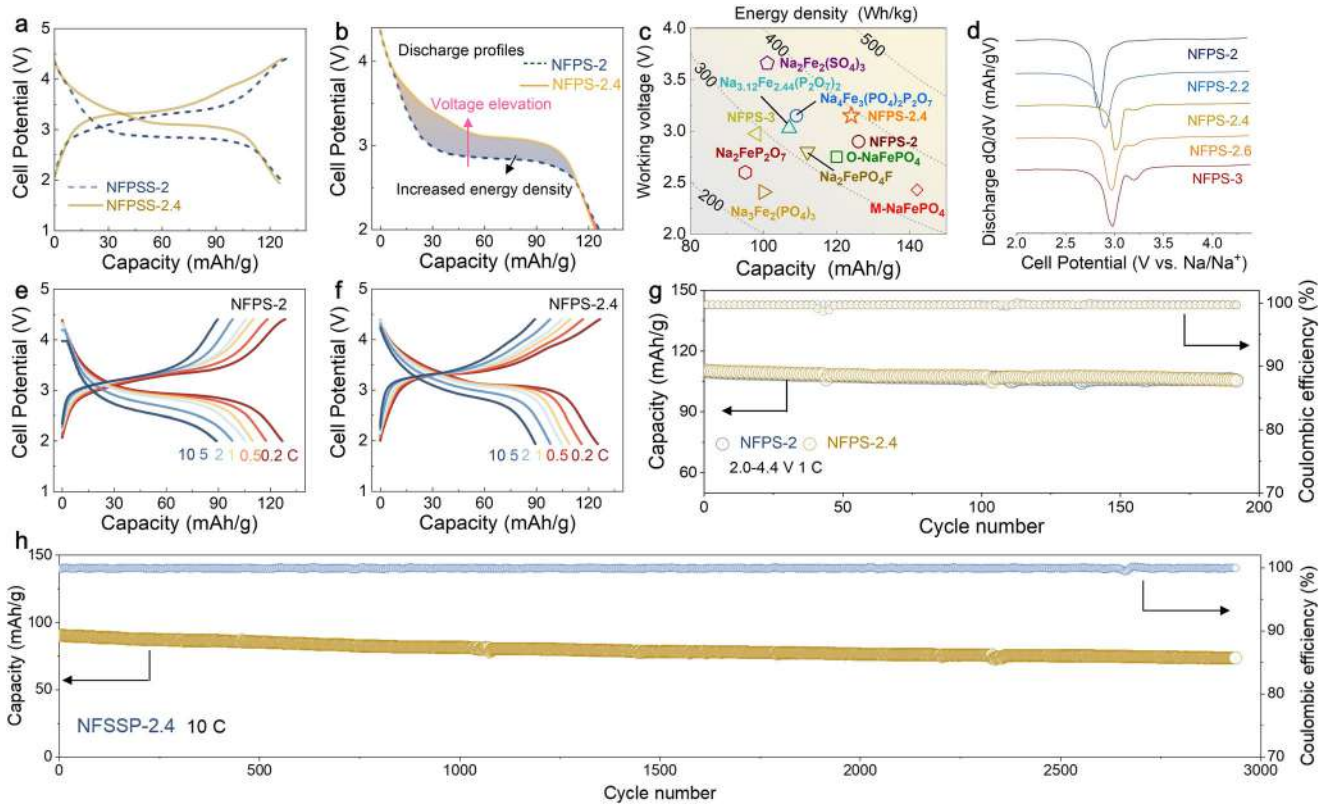



**Fig. 3 | Electrochemical performance in half cells. a** The typical charge/discharge curves of NFPS-2 and NFPS-2.4 electrodes. **b** The voltage elevation and energy density increase of NFPS-2.4 *vs.* NFPS-2. **c** The comparison of working voltage, capacity, and energy density in various iron-based polyanion cathodes for NIBs. **d** The discharging dQ/dV curves of $Na_{1-x}Fe_2(PO_4)_{1-x}(SO_4)_{2+x}$ family. The charging/discharging profiles of NFPS-2 (**e**) and NFPS-2.4 (**f**) electrodes in various C-rates. **g** The cycling performance comparison between NFPS-2and NFPS-2.4 electrodes at 1 C. **h** The long-term cycling performance of NFPS-2.4 electrodes at high rate of 10 C between 2 and 4.4 V.

$_xFe_2(PO_4)_{1-x}(SO_4)_{2+x}$, the discharge voltage plateau gradually elevates with increase of $SO_4$ groups. However, with the further increase of $x$ to 0.6 and 1, NFPS-2.6 and NFPS-3 deliver the lowered discharge voltage instead, which is mainly ascribed to their relatively large electrochemical polarization (Fig. S17). The structure symmetrical variation should be mainly responsible for kinetics deterioration. Such a voltage variation trend is comprehensively determined by the induced effects from $SO_4$ group and electrochemical kinetics aspects[40]. Despite the enhanced induced effects, due to introduction of excess $SO_4$ groups in NFPS-2.6 and NFPS-3, the serious Na sites metastability and limited $Na^+$ mobility have led to voltage hysteresis and cell potential lowering[22]. Besides, we find that the capacities of NFPS-2, NFPS-2.2 and NFPS-2.4 are obviously higher than those of NFPS-2.6 and NFPS-3, which can be attributed to the lowered redox activity caused by limited $Na^+$ migration kinetics when excess $SO_4$ groups introduced in NFPS-2.6 and NFPS-3. Therefore, NFPS-2.4 shows the highest energy density among $Na_{1-x}Fe_2(PO_4)_{1-x}(SO_4)_{2+x}$ family due to its large capacity and increased working voltage (Fig. S18). Furthermore, we measured the electrochemical impedance spectra (EIS) of several electrodes (Fig. S19 and Table S7), which indicates that the interfacial charge-transfer resistances ($R_{ct}$) of NFPS-2, NFPS-2.2 and NFPS-2.4 are basically at same level, but the $R_{ct}$ values for NFPS-2.6 and NFPS-3 increase significantly. We then assessed the rate performance of several cathodes from 0.2 to 10 C (Fig. S20). From Fig. 3e, f, we can find that NFPS-2.4 delivers a decent rate capability of 90 mA h $g^{-1}$ even at high current density of 10 C, which is comparable to that of NFPS-2. But it should be noted that NFPS-2.4 can realize significant voltage elevation at various C-rates, which is critical for high-energy NIBs towards practical application[41]. The galvanostatic intermittent titration technique (GITT) was employed to calculate the $Na^+$ ion diffusion coefficients ($D_{Na^+}$) of NFPS-2 and NFPS-2.4 electrodes during charging/discharging process (Fig. S21). Overall, two cathodes show the close $D_{Na^+}$ values in the plateau regions based on $Fe^{2+}/Fe^{3+}$ redox reaction, well consistent with their rate capability results. The $D_{Na^+}$ values vary from $10^{-13}$ to $10^{-11}$ $cm^2$ $s^{-1}$ during the whole de-/sodiation process, almost equivalent to that of the reported polyanionic phosphates[40,42]. The cycling performance of NFPS-2 and NFPS-2.4 were measured at 1 C (Fig. 3g and Fig. S22), which reveals that two electrodes deliver the capacity retention of 95% and the coulombic efficiency over 99.5% without obvious voltage degradation during ~200 cycles. More impressively, NFPS-2.4 was further cycled at high rate of 10 C for ~3000 times to demonstrate ~83% capacity retention (Fig. 3h), verifying its desirable cycling stability and good application prospects.

## Na storage mechanism

To provide comprehensive insights into the Na storage mechanism from structural aspects, the structure evolution of NFPS-2.4 electrode was recorded by in-situ XRD technique. Figure 4a displays series of XRD patterns at the selected angle range of (113), (024) and (116) diffraction peaks, in which the galvanostatic voltage-time profile within a complete charging and discharging process, as an inset was placed on the left side. Overall, these diffraction peaks can be indexed as the NASICON-typed structure framework, which exhibits the symmetrical shift, merger or separation, indicating NFPS-2.4 electrodes experience the reversible structure evolution between $Na_{2.6}Fe_2(PO_4)_{0.6}(SO_4)_{2.4}$ and $Na_{0.6}Fe_2(PO_4)_{0.6}(SO_4)_{2.4}$ phases during cycling. From the corresponding 2D contour plots of (113), (024) and (116) planes on the right side, we can more clearly find, in region I, the diffraction peaks slightly shift towards higher angles, which agrees with a solid solution mechanism[22]. With the further $Na^+$ extraction from the structure (region II), significant peak movement accompanied with the peak disappearance can be observed, suggesting a biphasic transition[22]. Upon the subsequent discharging process (region I' and II'), these diffraction peaks move leftward and recover, demonstrating the reversible $Na^+$ extraction and insertion

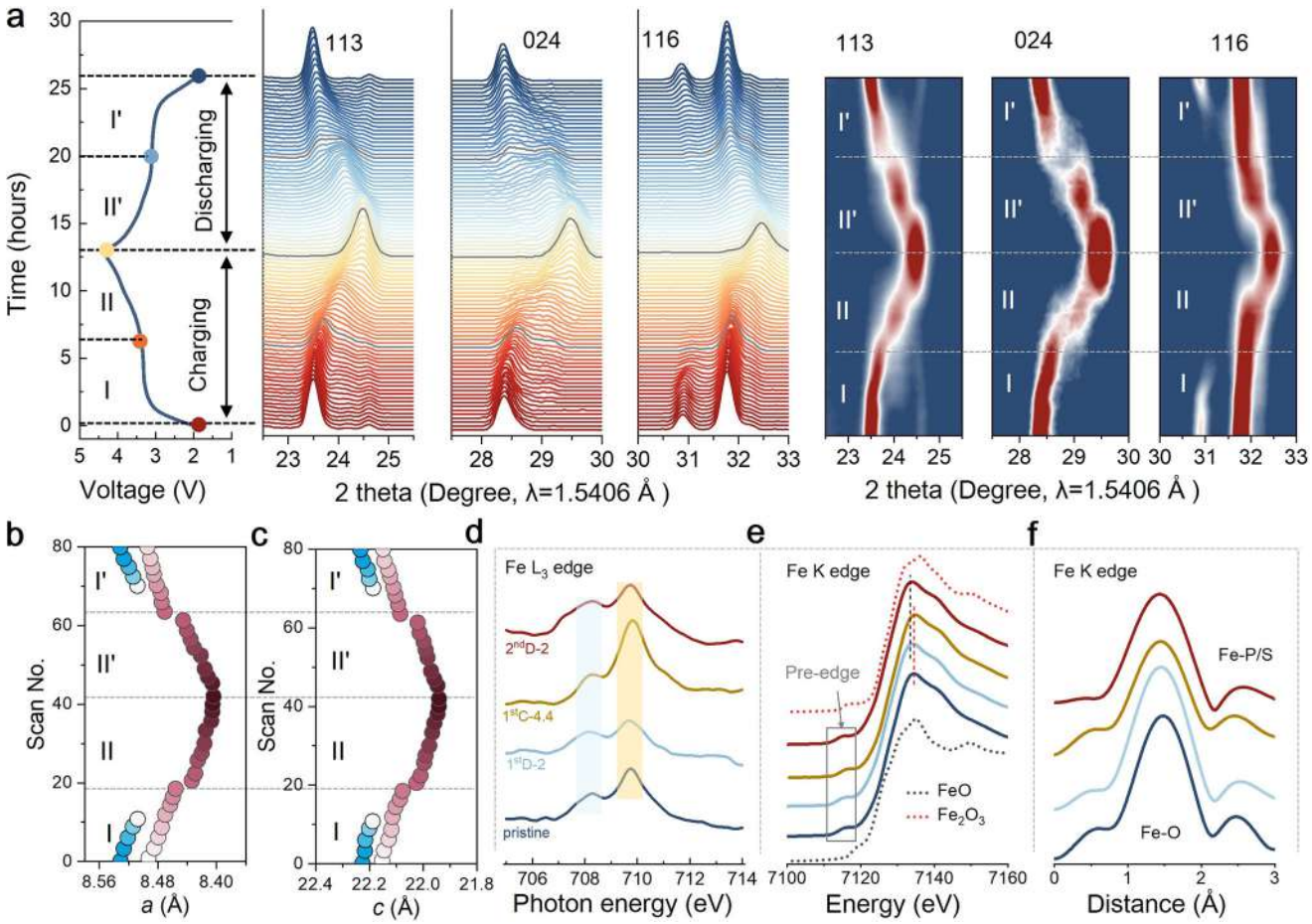



**Fig. 4 | Structure evolution and charge compensation. a** In-situ XRD patterns of NFPS-2.4 electrodes in the selected 2 theta angle range. The time-voltage profile was inserted on the left side. The 2D counter plots corresponding to (113), (024) and (116) planes were placed on the right sides. The calculated lattice parameter evolution of *a* (**b**) and *c* (**c**) within a complete charging/discharging process. **d** The ex-situ sXAS spectra at Fe L edges of NFPS-2.4 electrodes under different states of charge. The ex-situ XANES (**e**) and EXAFS (**f**) spectra at Fe K edges of NFPS-2.4 electrodes during (de)sodiation.

behavior. Such an electrochemical mechanism with the combination of solid-solution and bi-phase transition has also been demonstrated in NFPS-2 electrodes. The corresponding variations in structure parameters of *a* and *c* for NFPS-2.4 electrodes during charging and discharging process were described in Fig. 4b, c, respectively, which contributes to the total volume change of ~3.3% based on the fully sodiated and desodiated states (Fig. S23). The reversible structure evolution with small contraction or expansion in cell units is mainly responsible for the desirable cycling performance of NFPS-2.4 electrodes.

The charge compensation of iron reaction center of NFPS-2.4 electrodes was disclosed by combining various X-ray spectra analysis, in which the measured electrodes were in different states of charge, including the pristine state (open circuit voltage state), pre-discharging to 2.0 V ($1^{st}$ D-2), charging to 4.4 V ($1^{st}$ C-2) and the second discharging to 2.0 V ($2^{nd}$ D-2). The ex-situ sXAS spectra shows two characteristic peaks at Fe $L_3$ edges (Fig. 4d), which are located at ~708 eV ($L_3$ low, marked by blue band) and ~710 eV ($L_3$ high, marked by yellow band), respectively[43]. When NFPS-2.4 electrode is at a pristine state, the intensity of $L_3$-high peak is far higher than that of $L_3$-low peak, revealing trivalent oxidation state of iron. Upon pre-charged to 2.0 V, the relative intensity for $L_3$-low peak increases but that of $L_3$-high peak decreases, indicating the iron reduction from +3 to +2. After further charging to 4.4 V, the $L_3$-high peak increases significantly, implying that $Fe^{2+}$ is fully oxidized to $Fe^{3+}$ with two mole $Na^+$ extraction from structure. As the electrode continuously discharged to 2.0 V in the second cycle, $L_3$-low peak increases again, indicating trivalent iron is in turn reduced to bivalent with reversible insertion of two mole $Na^+$ into structure. The reversible reduction/oxidation in terms of $Fe^{2+}/Fe^{3+}$ couples in NFPS-2.4 electrodes during charging and discharging process was also demonstrated by the ex-situ XPS results (Fig. S24). Furthermore, the X-ray absorption near-edge structure (XANES) and extended X-ray absorption fine structure (EXAFS) analysis were carried out to reveal the coordination environment evolution during electrochemical reaction. As shown in Fig. 4e, the XANES spectra of $Fe_2O_3$ and FeO at K edges were employed for references of $Fe^{3+}$ and $Fe^{2+}$, respectively[10]. It can be found that Fe K edges of NFPS-2.4 electrodes shifted towards the lower energy position in the pre-discharging process, then moved rightward upon charging to 4.4 V and eventually returned to FeO energy location, confirming the reversible $Fe^{2+}/Fe^{3+}$ redox during charging and discharging process[42]. More importantly, the peak intensities at Fe pre-edge of NFPS-2.4 electrodes have hardly changed at various states of charge (marked by the gray rectangle), indicating no significant distortion or deformation of $FeO_6$ octahedral coordination during sodiation/desodiation[16]. The chemical coordination reversibility of iron reaction center in NFPS-2.4 electrodes was also reflected in the EXAFS spectra (Fig. 4f). Only slight intensity and interatomic distance changes can be observed in the Fe-O and Fe-P/S spectra between the fully charged (4.4 V) and discharged states (2.0 V), suggesting desirable structure and coordination reversibility of NFPS-2.4 electrodes during $Fe^{2+}/Fe^{3+}$ redox process[32].

### Air stability and full-cell performance

Since sulfates are prone to generate hydrated phase impurities due to the hygroscopic feature of $SO_4^{2-}$ anions[19], we pay more attention to the

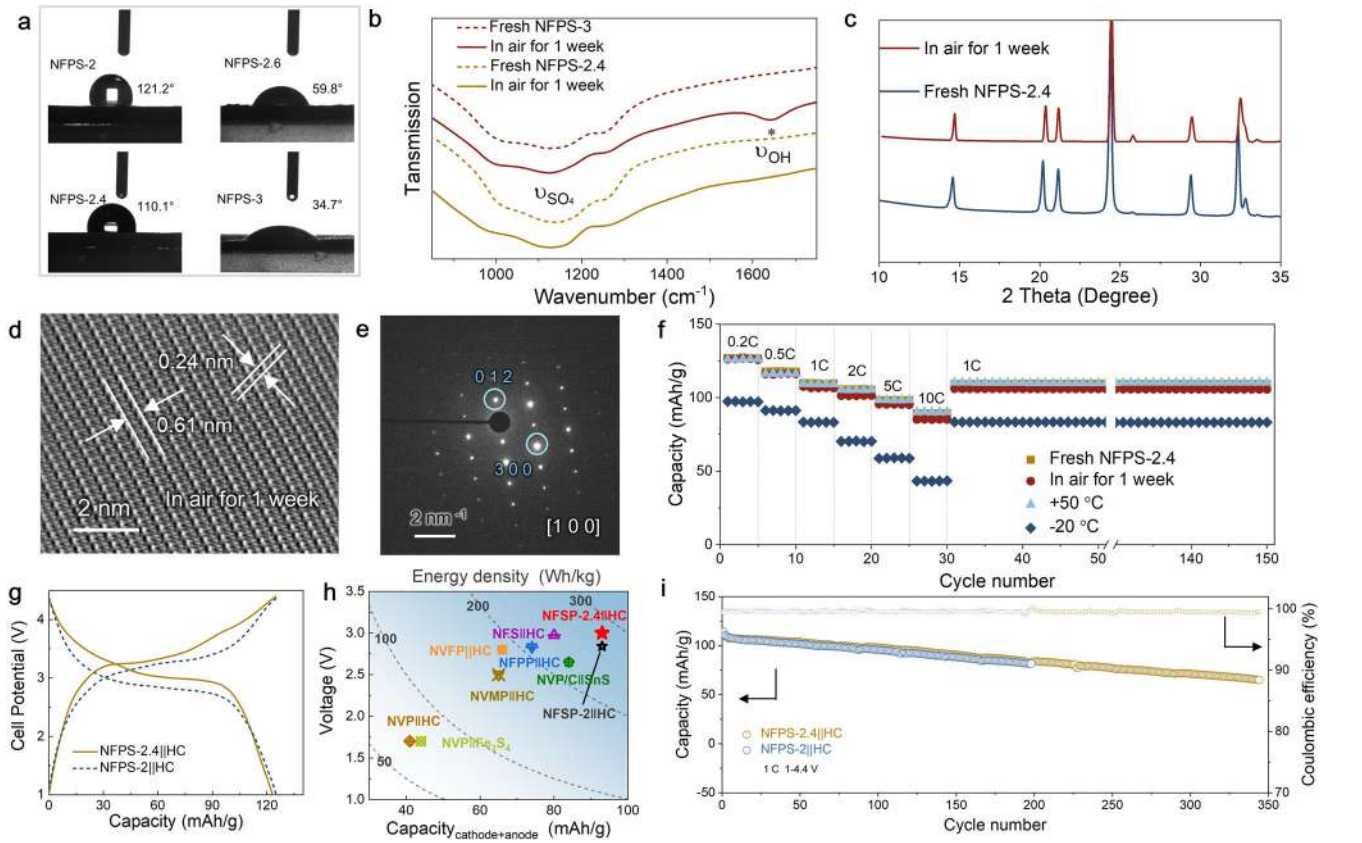



**Fig. 5 | Structure stability, high-low temperature and full-cell performance. a** The contact angles comparison of NFPS-2, NFPS-2.4, NFPS-2.6 and NFPS-3 surfaces. **b** The FTIR spectra of NFPS-2.4 and NFPS-3 cathodes before and after exposing to air for one week. **c** The XRD comparison of NFPS-2.4 cathodes between fresh and exposed ones. The HRTEM images (**d**) and SAED patterns (**e**) of NFPS-2.4 samples after storage in air for one week. **f** The electrochemical performance comparison of NFPS-2.4 electrodes under various conditions. **g** The charging/discharging profiles of NFPS-2 | | HC and NFPS-2.4 | | HC full-cell configurations. **h** The energy density, working voltage, capacity of various polyanionic cathodes-based full cells calculated by the total mass of cathode and anodes. **i** The cycling performance of NFPS-2 | | HC and NFPS-2.4 | | HC at 1 C.

hygroscopicity/ hydrophobicity of $Na_{1-x}Fe_2(PO_4)_{1-x}(SO_4)_{2+x}$ ($0 \le x \le 1$) family with high proportion of $SO_4$ groups in structure. Figure 5a compares the measured static contact angles by using deionized water to drop on surfaces of NFPS-2, NFPS-2.4, NFPS-2.6 and NFPS-3 electrodes. It can be observed that the contact angle gradually decreases with the more $SO_4$ groups in structure. Particularly, NFPS-2.4 shows a contact angle of 110° belonging to the lyophobic surface (>90°), indicating its large moisture absorption resistance. In contrast, the contact angles of NFPS-2.6 (59.8°) and NFPS-3 (34.7°) are less than 90°, which implies that they are more easily wetted by the water because of excessive $SO_4^{2-}$ anions in the structures. Considering the good hydrophobicity, we further investigate the chemical stability of NFPS-2.4 cathodes when exposed to air with moisture (relative humidity of ~60%). Figure 5b exhibits the FTIR spectra of NFPS-2.4 and NFPS-3 samples before and after exposure to air for one week. NFPS-3 exhibits an obvious stretching vibration reflection of O–H bond caused by the adsorbed water in ~1650 $cm^{-1}$ after exposure to air. However, no peak signals assigned to water can be observed for NFPS-2.4 samples even in air for one week, indicating its positive air stability. The O1s XPS spectra discloses the main peaks at ~530 eV corresponding to the lattice oxygen (*i.e.*, P/S-O in structure) for both NFPS-2.4 and NFPS-3 cathodes (Fig. S26). After exposure to air, a new peak of O-H bond appears in the O1s XPS spectra of NFPS-3 cathode (Fig. S26a), illustrating generation of hydrate phase on the surface. No additional XPS signals can be observed in NFPS-2.4 cathode in air (Fig. S26b), further confirming its good storage stability. Figure 5c describes XRD comparison of NFPS-2.4 cathodes before and after exposing to air, which shows no obvious peak shifts and changes, validating desirable structural stability. On the contrary, the hydrate-sulfate phase in NFPS-3 cathode can be observed after contacting the moisture in air (Fig. S26). Moreover, the high-resolution transmission electron microscopy (HRTEM) images and the corresponding SAED patterns reveal that some amorphous and poor crystalline regions have formed in the exposed NFPS-3 cathodes (Fig. S27), which can be assigned to the hydrate-sulfate impurities. As for NFPS-2.4 sample after exposure to air, its HRTEM and SAED images unveil clear lattice fringes and regular electron diffraction spots belonging to (012) and (300) planes (Fig. 5d, e), further demonstrating the well-maintained structural integrity. In addition, the pure NFPS-2.4 powder was subjected to heat treatment from 30 °C to 800 °C in air (Fig. S28), which discloses a starting decomposition of material at ~600 °C, hinting its favorable thermal stability[30].

Figure 5f shows the electrochemical performance of NFPS-2.4 cathodes under various conditions. It can be found that NFPS-2.4 cathodes deliver almost the same reversible capacities at 0.1 C before and after exposing themselves to air (Fig. S29), indicating good air stability. At the high rate of 10 C, a capacity of ~85 mA h $g^{-1}$ can be still achieved for the exposed samples, which are comparable to that of fresh ones (90 mA h $g^{-1}$). As the C-rate further returned to 1 C, both fresh and exposed electrodes can be stably cycled for over 120 times without capacity fading. Besides, we can't observe any performance differences of NFPS-2.4 electrodes between room temperature and high temperature of 50 °C, indicating the superior rate performance can be preserved in hot climate conditions. In the case of low temperature of −20 °C, the reversible capacity decreases to 98 mA h $g^{-1}$ from 125 mA h $g^{-1}$ (room temperature), which could be associated with low electrochemical activity caused by the limited ion conduction of the electrolyte at low temperatures. However, NFPS-2.4 electrodes can still obtain

44 mA h $g^{-1}$ capacity at 10 C rate under -20 °C condition, attesting that low temperature does not deteriorate the properties of the material itself except for the external kinetics factors. To verify the practical application prospects of NFPS-2.4 cathodes, the full cell configurations were fabricated using our reported hard carbon (HC) as anodes[44]. The Na storage behavior of HC is presented in Figure S30, which reveals a reversible capacity of ~385 mA h $g^{-1}$ with the initial Coulombic efficiency of 87.5% in the voltage range of 0-2 V. The pre-discharged positive electrodes were matched with HC negative electrodes at a N/P mass ratio of 1:3. Figure 5g exhibits the typical charging/discharging profiles of NFPS-2 | | HC and NFPS-2.4 | | HC full cells between 1–4.4 V, respectively. The reversible capacities of two full cells are close to reach 123 mA h $g^{-1}$, which are comparable to those in their half cells (~125 mA h $g^{-1}$). However, the increased $Fe^{2+}/Fe^{3+}$ redox voltage from the appropriate induced effects in NFPS-2.4 cathodes would lead to the increased energy density in full cells. We summarized the energy densities of NFPS-2.4 and other representative polyanion-type cathodes-based full cells calculated by the total masses of cathode and anode in (Fig. 5h). We can find that NFPS-2.4 | | HC achieves an energy density of ~278 W h $kg^{-1}$ (Fig. S31), far exceeding that of other typical polyanionic full-cell systems[8,45–49]. A higher electrode loading level and solid-state batteries technologies are welcomed using $Na_{1-x}Fe_2(PO_4)_{1-x}(SO_4)_{2+x}$ ($0 \le x \le 1$) family as cathodes for exploring the possibilities of practical applications of NIBs. NFPS-2 | | HC and NFPS-2.4 | | HC full cells were further cycled at 1 C to reveal the capacity retention of ~74% after 200 cycles and keep the high Coulombic efficiency approaching 100% for each cycle (Fig. 5i and Fig. S32), demonstrating the desirable cycling stability.

## Discussion

In summary, we systematically investigated the effects of the relative ratio of $SO_4/PO_4$ polyanion groups on the structures, electrochemical behavior and kinetics aspects of $Na_{1-x}Fe_2(PO_4)_{1-x}(SO_4)_{2+x}$ ($0 \le x \le 1$) family. With introduction of more $SO_4$ group in structure, the Fe-O covalency decreases due to stronger induced effects and the $Na^+$ diffusion dynamics lowers due to structural symmetry destruction. The $Fe^{2+}/Fe^{3+}$ redox potential in $Na_{1-x}Fe_2(PO_4)_{1-x}(SO_4)_{2+x}$ ($0 \le x \le 1$) family is comprehensively determined by the Fe-O covalency and $Na^+$ migration kinetics. Theoretical calculation and experimental characterization indicate that NFPS-2, NFPS-2.2 and NFPS-2.4 can maintain high structure symmetry and favorable $Na^+$ migration kinetics, but NFPS-2.6 and NFPS-3 show sluggish kinetics properties. Due to the enhanced induced effects without deteriorating dynamics, NFPS-2.4 deliver high average discharging voltage of ~3.2 V and desirable energy density of ~400 W h $kg^{-1}$, higher than those of the representative iron-based polyanion cathodes for NIBs. NFPS-2.4 electrode experienced reversible $Fe^{2+}/Fe^{3+}$ redox process and small cell volume change of ~3.3% within a complete charging and discharging process, which was responsible for superior electrochemical performance. Besides, NFPS-2.4 cathode also exhibits positive air stability, wide temperature adaptability and good full-cell performance, showing some application potentials toward practical NIBs.

## Methods

### Sample preparation

NASICON-structure $Na_{1-x}Fe_2(PO_4)_{1-x}(SO_4)_{2+x}$ ($0 \le x \le 1$, *e.g.*, $x = 0, 0.2, 0.4, 0.6$ and 1, denoted as NFPS-2, NFPS-2.2, NFPS-2.4, NFPS-2.6 and NFPS-3) family were prepared via a facile solid-state method. First, stoichiometric mixtures of $NaNO_3$, $Fe(NO_3)_3 \bullet 9H_2O$, $(NH_4)_2SO_4$ and $NH_4H_2PO_4$ were in turn dissolved in 60 ml of $H_2O$. After stirring the mixed solution at 120 °C until evaporation of water, the obtained precursor was then sintered at 550 °C (the heating rate is about 5 °C $min^{-1}$) for 12 h under air to get pure cathode materials. For carbon coating to improve electronic conductivity, these cathodes were mixed with Ketjen black (KB) carbon in a weight ratio of 96:4 via high energy ball milling. The filling ratio of zirconium ball milled beads is about 30% in each 150 mL jar. The ball-milling machine was set to be 400 rpm to mill for 12 h to obtain the final samples. All the regents with analytical purity were purchased from Sigma-Aldrich.

### Material characterizations

The crystal structure of samples was characterized by X-ray diffractometer (XRD, Cu Kα, λ = 1.5406 Å). A scanning transmission electron microscopy (STEM, JEM-ARM 200 F) was employed to acquire structure details of samples. Morphologies and element composition of as-prepared materials were investigated using a field emission scanning electron microscope (SEM, JEOL JSM-7500FA) with energy-dispersive spectroscope (EDS) accessories. Thermogravimetry (TG) and derivatives of thermal gravity (DTG) were conducted by a thermogravimetric analyzer (DTA6300). The X-ray photoelectron spectroscopy (XPS, Al Kα) and inductively coupled plasma-optical emission spectroscopy (ICP-OES, 730 ES) were employed to determine the elements valence and composition of samples. $^{57}Fe$ Mössbauer spectral measurements were performed at Halder-type spectrometer (ARL4460). The functional group and structure features were characterized by Fourier-transform infrared spectroscopy (FTIR, T27) and Raman spectra (Laser GS6000). The soft- X-ray absorption spectroscopy (sXAS) were recorded at beamline at National Synchrotron Radiation Laboratory (Hefei China, 2024-HLS-PT-007925). X-ray absorption near-edge structure (XANES) spectra was acquired at the P64 XAS beamline of the DESY synchrotron. High resolution transmission electron microscopy (HRTEM, JSM-7001F) was carried out to obtain lattice fringes and selected-area electronic diffraction (SAED) of samples. The in-situ XRD was collected at the P02.1 Powder Diffraction beamline.

### Electrochemical measurements

To fabricate cathode electrodes, the active materials, Ketjenblack (KB) and poly(tetrafluoroethylene) (PTFE) binder at a mass ratio of 7:2:1 were strictly ground and mixed, followed by a sufficient rolling procedure until formation of an evenly mixed electrode thin film. The as-obtained electrode film is then cut into 6 × 6 mm square electrodes and ensures that the loading content of active substance is about 5 mg $cm^{-2}$. The hard carbon (HC) electrode consists of HC materials, acetylene black and poly-(vinylidenefluoride) (PVDF) at a mass ratio of 8:1:1. For half-cell, the 2032 coin-type cells were assembled in the glove box full of Ar ($H_2O$ and $O_2$ concentration less than 0.01 ppm), employing Na metal as counter, glass fiber as separator and 1 M $NaClO_4$ in propylene carbonate (PC) with 5% fluoroethylene carbonate (FEC) additive as electrolyte. The galvanostatic charge/discharge measurements from 0.2 to 10 C between 2 to 4.4 V were performed on a Land/Neware battery testing system, where 1 C represents the current density of 120 mA $g^{-1}$. The capacities presented in this work were calculated based on the active materials (which have been deducted the coating carbon weight). For fabrication of full cells, all procedures and use of electrolytes are the same as half-cell assembly except for the utilization of the hard carbon electrode as counter. The voltage window for the full cell is within 1–4.4 V. For the galvanostatic current intermittent titration technology (GITT) measurements, all electrodes are charged or discharged (0.1 C) for 10 min followed by a rest of 60 min to obtain a nearly steady state. Electrochemical impedance spectroscopy (EIS) was determined in the frequency range of 100 kHz to 100 mHz via an electrochemical workstation (Z ahner, IM6).

### Calculation method

First principles calculations were conducted via the Vienna ab initio simulation package (VASP) based on density functional theory (DFT). The unit cell parameters and position of each atom were fully optimized under the Hubbard corrected DFT (DFT + U) within the ferromagnetic state until the ultimate residual force was no more than 0.05 eV per atom. For all DFT calculations, cell parameters and atomic positions were fully relaxed to achieve optimized crystal structures. The exchange-correlation interaction was described with the generalized gradient approximation (GGA) according to Perdew–Burke–Ernzerhof (PBE). A cut-off kinetic energy of 400 eV was used for all calculation processes. The 20 models with the lowest electrostatic energies were adopted to carry out structural relaxation through first principles calculations. The most stable structure was chosen

for the subsequent simulations. The max force on each atom to relax in the geometry was 0.1 $eVÅ^{-1}$. All the conducted calculations were performed using periodic boundary conditions, and the corresponding Brillouin-zone integrations were performed using a $3 \times 3 \times 3$ Monkhorst–Pack grids. The migration barriers were determined using nudged elastic band (NEB) method and GGA PBE without U as implemented in VASP.

## Data availability

All data supporting the findings of this study are available within the paper and its Supplementary Information.

Received: 26 January 2026; Accepted: 20 April 2026;
Published online: 03 June 2026

## References

1. Yang, Y. et al. Decoupling the air sensitivity of Na-layered oxides. *Science* **385**, 744–752 (2024).
2. Zhao, C. et al. Rational design of layered oxide materials for sodium-ion batteries. *Science* **370**, 708–711 (2020).
3. Hao, Z. et al. The distance between phosphate-based polyanionic compounds and their practical application for sodium-ion batteries. *Adv. Mater* **36**, 2305135 (2024).
4. Pan, H., Hu, Y.S. & Chen, L. Room-temperature stationary sodium-ion batteries for large-scale electric energy storage. *Energy Environ Sci.* **6**, 2338–2360 (2013).
5. Zhang, W. et al. Configurational entropy-tailored NASICON cathode redox chemistry for capacity-dense and ultralong cyclability. *Energy Environ. Sci.* **18**, 7278–7290 (2025).
6. Masquelier, C. & Croguennec, L. Polyanionic (phosphates, silicates, sulfates) frameworks as electrode materials for rechargeable Li (or Na) batteries. *Chem. Rev.* **113**, 6552–6591 (2013).
7. Wang, L. et al. Fast screening suitable doping transition metals to $Na_3V_2(PO_4)_2F_3$ for sodium-ion batteries with high energy density in wide-temperature range. *Adv Mater* **37**, 2505093 (2025).
8. Rui, X., Sun, W., Wu, C., Yu, Y. & Yan, Q. An advanced sodium-ion battery composed of carbon coated $Na_3V_2(PO_4)_3$ in a porous graphene network. *Adv Mater* **27**, 6670–6676 (2015).
9. Fan, D. et al. A novel NASICON-$Na_{3.4}MnV_{0.2}Cr_{0.2}Ti_{0.6}(PO_4)_3$ cathode with ultrahigh energy density and remarkable cycling stability toward practical Na-ion batteries. *Mater Today* **86**, 63–73 (2025).
10. Xu, C. et al. Reversible activation of $V^{4+}/V^{5+}$ redox couples in NASICON phosphate cathodes. *Adv. Energy Mater* **12**, 2200966 (2022).
11. Lu, X. et al. From lab to application: challenges and opportunities in achieving fast charging with polyanionic cathodes for sodium-ion batteries. *Adv Mater* **36**, 2407359 (2024).
12. Xu, C., Zhao, J., Yang, C. & Hu, Y.-S. Polyanionic cathode materials for practical Na-Ion batteries toward high energy density and long cycle life. *ACS Cent. Sci.* **9**, 1721–1736 (2023).
13. Wang, E. et al. Superstructure engineering enables NASICON-type phosphate cathodes with increased working voltage and energy density. *Adv. Mater* **37**, e12435 (2025).
14. Li, H. et al. A multielectron-reaction and low-strain $Na_{3.5}Fe_{0.5}VCr_{0.5}(PO_4)_3$ cathode for Na-Ion batteries. *ACS Energy Lett* **8**, 3666–3675 (2023).
15. Fang, Y. et al. High-performance olivine $NaFePO_4$ microsphere cathode synthesized by aqueous electrochemical displacement method for sodium ion batteries. *ACS Appl. Mater. Interfaces* **7**, 17977–17984 (2015).
16. Wang, H. et al. Constructing heterotransition metal ligand field clusters with a compact spatial structure for maintaining unimpeded sodium-ion migration. *ACS Nano* **19**, 34966–34980 (2025).
17. Cao, Y. et al. K-doped $Na_3Fe_2(PO_4)_3$ cathode materials with high-stable structure for sodium-ion stored energy battery. *J Alloy Compd* **784**, 939–946 (2019).
18. Huang, H. et al. Local electronic structure regulation enabling fluorophosphates cathode with improved redox potential and reversible capacity for sodium-ion batteries. *J Am Chem Soc* **146**, 28906–28913 (2024).
19. Liu, C. et al. Unlocking phase purity of sodium iron sulfate for low-cost and high-performance sodium-ion batteries. *J Am Chem Soc* **147**, 14635–14646 (2025).
20. Shiva, K., Singh, P., Zhou, W. & Goodenough, J. B. $NaFe_2PO_4(SO_4)_2$: a potential cathode for a Na-ion battery. *Energy Environ Sci* **9**, 3103–3106 (2016).
21. Gu, Z.Y. et al. Polyanionic cathodes for sodium-ion batteries: Materials, working mechanism, and applications. *Mater. Sci. Eng. R Rep.* **165**, 101008 (2025).
22. Chung, S.C., Ming, J., Lander, L., Lu, J. & Yamada, A. Rhombohedral NASICON-type $Na_xFe_2(SO_4)_3$ for sodium ion batteries: comparison with phosphate and alluaudite phases. *J Mater Chem A* **6**, 3919–3925 (2018).
23. Pinjari, S. D. et al. Site-selective Mg-doping regulated charge storage in $NaFe_2PO_4(SO_4)_2$ for high energy sodium-ion batteries. *Chem. Eng. J.* **493**, 152485 (2024).
24. Ben Yahia, H. et al. Sodium intercalation in the phosphosulfate cathode $NaFe_2(PO_4)(SO_4)_2$. *J. Power Sources* **382**, 144–151 (2018).
25. Shen, X. et al. Rapid mechanochemical synthesis of polyanionic cathode with improved electrochemical performance for Na-ion batteries. *Nat. Commun.* **12**, 2848 (2021).
26. Xu, C. et al. Guiding design of Mn-rich phosphate cathodes with less intrinsic antisite defects. *Angew Chem Int. Ed.* **64**, e202502758 (2025).
27. Hocking, R. K. et al. Fe L-Edge X-ray absorption spectroscopy determination of differential orbital covalency of siderophore model compounds: electronic structure contributions to high stability constants. *J. Am. Chem. Soc.* **132**, 4006–4015 (2010).
28. Hao, Z.L. et al. Heterogeneous-interface-induced charge redistribution toward Fe-based polyanion cathode for advanced sodium-ion batteries. *J Am Chem Soc* **147**, 13905–13914 (2025).
29. Ren, M. et al. Homeostatic solid solution in layered transition-metal oxide cathodes of sodium-ion batteries. *J Am Chem Soc* **145**, 224–233 (2022).
30. Grebenshchikova, A. et al. NaSICON $NaFe_2PO_4(SO_4)_2$ revisited: insights into the crystal structure and electrochemical performance. *ACS Appl. Energy Mater.* **8**, 13620–13630 (2025).
31. Chen, M. et al. NASICON-type air-stable and all-climate cathode for sodium-ion batteries with low cost and high-power density. *Nat. Commun.* **10**, 1480 (2019).
32. Xu, C. et al. Development of high-performance iron-based phosphate cathodes toward practical Na-Ion batteries. *J. Am. Chem. Soc.* **146**, 9819–9827 (2024).
33. Deng, S. et al. Coordination chemistry regulation suppressing voltage hysteresis for $Na_3MnTi(PO_4)_3$ in high-rate sodium-ion batteries. *ACS Nano* **19**, 10381–10391 (2025).
34. Kim, J. et al. Unexpected discovery of low-cost maricite $NaFePO_4$ as a high-performance electrode for Na-ion batteries. *Energy Environ. Sci.* **8**, 540–545 (2015).
35. Xiao, J.C. et al. Identifying the β-to-α phase transition during the long cycling process in $Na_2FePO_4F$ cathode. *Energy Storage Mater* **73**, 103781 (2024).
36. Chen, M. et al. A novel graphene oxide wrapped $Na_2Fe_2(SO_4)_3$/C cathode composite for long life and high energy density sodium-ion batteries. *Adv. Energy Mater* **8**, 1800944 (2018).
37. Zhao, A. et al. A novel Fe-defect induced pure-phase $Na_4Fe_{2.91}(PO_4)_2P_2O_7$ cathode material with high capacity and ultra-long lifetime for low-cost sodium-ion batteries. *Nano Energy* **91**, 106680 (2022).
38. Liu, Y. et al. The structural origin of enhanced stability of $Na_{3.32}Fe_{2.11}Ca_{0.23}(P_2O_7)_2$ cathode for Na-ion batteries. *Nano Energy* **79**, 105417 (2021).
39. Wang, J. et al. Fe-rich pyrophosphate with prolonged high-voltage-plateaus and suppressed voltage decay as sodium-ion battery cathode. *Nano Energy* **116**, 108822 (2023).

40. Liu, Y. et al. Identifying the intrinsic anti-site defect in manganese-rich NASICON-type cathodes. *Nat Energy* **8**, 1088–1096 (2023).
41. Setiawati, E., Hayashi, M., Tsuda, M., Hayashi, K. & Kobayashi, R. Electrochemical properties of carbon-composite NASICON-type iron sulfate $Fe_2(SO_4)_3$ as a cathode for lithium secondary batteries. *J. Power Sources* **244**, 207–213 (2013).
42. Song, W. et al. Mechanistic insights into enhanced capacity and pure-phase formation in Fe-based mixed phosphate cathodes. *J. Am. Chem. Soc.* **147**, 39151–39159 (2025).
43. Xu, C. et al. A novel NASICON-Typed $Na_4VMn_{0.5}Fe_{0.5}(PO_4)_3$ cathode for high-performance Na-Ion batteries. *Adv. Energy Mater.* **11**, 2100729 (2021).
44. Feng, G. et al. Microbially glycolysis-regulated hard carbons for sodium-ion batteries. *Nano Energy* **136**, 110728 (2025).
45. Liu, Y. et al. Insight into the multirole of graphene in preparation of high performance $Na_{2+2x}Fe_{2-x}(SO_4)_3$ cathodes. *ACS Sustain Chem. Eng.* **6**, 16105–16112 (2018).
46. Lu, F. et al. New-type NASICON-$Na_4FeV(PO_4)_3$ cathode with high retention and durability for sodium ion batteries. *Carbon* **196**, 562–572 (2022).
47. Li, H. et al. Rational architecture design enables superior Na storage in greener NASICON-$Na_4MnV(PO_4)_3$ cathode. *Adv. Energy Mater.* **8**, 1801418 (2018).
48. Mao, K. et al. Precursor-free synthesis of $Na_4Fe_3(PO_4)_2P_2O_7$ cathode directly from metallic iron for sodium-ion batteries. *Small* **21**, e10368 (2025).
49. Cao, X. et al. Nanoflake-constructed porous $Na_3V_2(PO_4)_3$/C hierarchical microspheres as a bicontinuous cathode for sodium-ion batteries applications. *Nano Energy* **60**, 312–323 (2019).


## Acknowledgements

J.Z. discloses support for the research of this work from National Natural Science Foundation of China (Grant No. 92472201) and the Strategic Priority Research Program of Chinese Academy of Sciences (XDA0400202). X.G. discloses support for the research of this work from National Natural Science Foundation of China (Grant No. 22425804). W.Y. discloses support for the research of this work from National Natural Science Foundation of China (Grant No. 52372228). C.X. discloses support for the research of this work from National Natural Science Foundation of China (Grant No. 22309203), the Sichuan Science and Technology Program (Grant No. 2025ZNSFSC0364), the Fundamental Research Funds for the Central Universities (Grant No. 2682025CX145) and the China Postdoctoral Science Foundation founded Project (Grant No. 2025T180291, 2024M762671). Y. L. gratefully acknowledges financial support from the Swedish Energy Agency (Nos. P2022-00055 and P2023-00603) and StandUP for Energy, Sweden.

## Author contributions

C.X., W.Y., X.G., J.Z. and Y.H. conceived the experiments and wrote the paper. Y.L. performed XAS experiment. G.F., Z.C., X.L. and Z.W. assisted in conducting data analyses. All authors have read and approved the manuscript.

## Competing interests

The authors declare no competing interests.

## Additional information

**Supplementary information** The online version contains supplementary material available at https://doi.org/10.1038/s44456-026-00006-4.

**Correspondence** and requests for materials should be addressed to Weiqing Yang, Xiaodong Guo, Junmei Zhao or Yong-Sheng Hu.

**Reprints and permissions information** is available at http://www.nature.com/reprints

**Publisher's note** Springer Nature remains neutral with regard to jurisdictional claims in published maps and institutional affiliations.

**Open Access** This article is licensed under a Creative Commons Attribution-NonCommercial-NoDerivatives 4.0 International License, which permits any non-commercial use, sharing, distribution and reproduction in any medium or format, as long as you give appropriate credit to the original author(s) and the source, provide a link to the Creative Commons licence, and indicate if you modified the licensed material. You do not have permission under this licence to share adapted material derived from this article or parts of it. The images or other third party material in this article are included in the article's Creative Commons licence, unless indicated otherwise in a credit line to the material. If material is not included in the article's Creative Commons licence and your intended use is not permitted by statutory regulation or exceeds the permitted use, you will need to obtain permission directly from the copyright holder. To view a copy of this licence, visit http://creativecommons.org/licenses/by-nc-nd/4.0/.

© The Author(s) 2026